

See discussions, stats, and author profiles for this publication at: <https://www.researchgate.net/publication/353826129>

Precipitation of γ'' in Inconel 718 alloy from microstructure to mechanical properties

Article in *Materialia* · August 2021

DOI: 10.1016/j.mtla.2021.101187

CITATIONS

22

READS

218

10 authors, including:



Michel Perez

Institut National des Sciences Appliquées de Lyon

170 PUBLICATIONS 4,723 CITATIONS

[SEE PROFILE](#)



Thibaut Chaise

Institut National des Sciences Appliquées de Lyon

54 PUBLICATIONS 902 CITATIONS

[SEE PROFILE](#)



S. Cazottes

Institut National des Sciences Appliquées de Lyon

91 PUBLICATIONS 1,167 CITATIONS

[SEE PROFILE](#)



Didier Bardel

Framatome

41 PUBLICATIONS 503 CITATIONS

[SEE PROFILE](#)



Precipitation of γ in Inconel 718 alloy from microstructure to mechanical properties

Alexandre Balan, Michel Perez, Thibaut Chaise, Sophie Cazottes, Didier Bardel, Fabien Corpace, François Pichot, Alexis Deschamps, Frédéric de Geuser, Daniel Nelias

► To cite this version:

Alexandre Balan, Michel Perez, Thibaut Chaise, Sophie Cazottes, Didier Bardel, et al.. Precipitation of γ in Inconel 718 alloy from microstructure to mechanical properties. *Materialia*, 2021, 20, pp.101187. 10.1016/j.mtla.2021.101187 . hal-03366225

HAL Id: hal-03366225

<https://hal.science/hal-03366225>

Submitted on 11 Oct 2021

HAL is a multi-disciplinary open access archive for the deposit and dissemination of scientific research documents, whether they are published or not. The documents may come from teaching and research institutions in France or abroad, or from public or private research centers.

L'archive ouverte pluridisciplinaire **HAL**, est destinée au dépôt et à la diffusion de documents scientifiques de niveau recherche, publiés ou non, émanant des établissements d'enseignement et de recherche français ou étrangers, des laboratoires publics ou privés.

Precipitation of γ'' in Inconel 718 alloy from microstructure to mechanical properties.

Alexandre Balan^{a,b,1}, Michel Perez^{b,*}, Thibaut Chaise^a, Sophie Cazottes^b, Didier Bardel^{a,b,2}, Fabien Corpacci^d,
François Pichot^d, Alexis Deschamps^c, Frédéric De Geuser^c, Daniel Nelias^a

^aUniv Lyon, INSA-Lyon, CNRS UMR5259, LaMCoS, F-69621, France

^bUniv Lyon, INSA Lyon, UCBL, CNRS, MATEIS, UMR5510, 69621 Villeurbanne, France

^cUniv. Grenoble Alpes, CNRS, SIMAP, F-38000 Grenoble, France

^dSafran Aircraft Engines, Safran-Group, Evry-Corbeil plant, 91003 Evry France

Abstract

This paper presents a coupled approach able to describe γ'' precipitation evolution and associated yield strength after various heat treatments in Inconel 718 alloy. The precipitation state is modeled *via* the implementation of classical nucleation and growth theories for plate-shaped particles. The precipitation model is validated through small-angle neutron scattering and transmission electron microscopy experiments. The precipitation size distribution serves as an input parameter to model the yield strength using a micromechanical model based on shear and bypass mechanisms accounting for the particular shapes of the precipitates. Results are in good agreement with measured yield stresses for various precipitation states. A complete simulated TTT diagram of the γ'' phase with the associated yield strength is proposed. The coupled model is finally applied to a series of non-isothermal treatments representative of welding (or additive manufacturing) from the peak aged state.

Keywords: Alloy (Inconel) 718, γ'' phase, Precipitation kinetics, Kampmann-Wagner Numerical (KWN) modeling, Scanning electron microscopy (SEM), Small Angle Neutron Scattering, Structural hardening alloys

1. Introduction

Inconel 718 is a nickel base superalloy mainly used in the aerospace industry to produce critical components for turbines, thanks to its excellent mechanical properties and corrosion resistance at high temperature [1]. Moreover, its good weldability, relative to other superalloys, makes it a very good candidate for assembly parts [2].

Welding or additive manufacturing processes are very complex processes during which the material is subjected to extreme thermomechanical loading, which involves microstructural evolution as grain growth and precipitation (or dissolution) of hardening phases. To optimize the final material properties it is essential to follow the evolution of the microstructure and mechanical properties in the Heat Affected Zone (HAZ).

Its outstanding mechanical properties are due to the fine precipitation of homogeneous hardening inter-metallic phases in the nickel solid solution γ . These precipitates are the $L1_2$ face-centered cubic (fcc) structure γ' ($\text{Ni}_3(\text{Ti},\text{Al})$) and DO_{22} body centered tetragonal (bct) structure γ'' (Ni_3Nb). The latter has the following orientation relationships [3]:

$$(001)_{\gamma''} \parallel \{001\}_{\gamma} \text{ and } [100]_{\gamma''} \parallel \langle 100 \rangle_{\gamma} \quad (1)$$

Oblak *et al.* [4] showed that γ' are coherent spherical precipitates and γ'' are coherent disc-shaped particles. This shape has been widely observed by numerous authors via TEM experiments; see [4–8] and more recently [9].

The characterisation of simultaneous γ' and γ'' precipitation is often complicated, as noted by Tian *et al.* [10]. These authors succeed in differentiating γ' and γ'' by using chemical contrast. They did not noted significant γ' precipitation after direct laser additive manufacturing. Several authors have noticed a co-precipitation phenomenon of γ' and γ'' particles. Kindrachuk *et al.* [11], in Inconel 706, and Philipps *et*

*Corresponding author.

Email address: Michel.Perez@insa-lyon.fr (Michel Perez)

¹Now at EDF Lab, Les Renardières, MMC Department, F-77250 Moret sur Loing, France.

²Now at Framatome, 10 rue Juliette Récamier, 69456 Lyon Cedex 06, France.

al. [12] in Inconel 718 have shown that the elastic energy of γ'/γ'' is lower than for each precipitate alone. The mechanisms of co-precipitation of these precipitates have been studied recently by Shi *et al.* [13] using phase-field modelling trying to determine the conditions under which the γ'' precipitation is favoured by pre-existing γ' particles. This mechanism is also observed by Detor *et al.* [14] who showed a precipitation of γ'' following γ' . More recently Theska *et al.* [15] have studied various sequences of γ'/γ'' precipitation, especially in the early stages of precipitation [16] and correlated it with the alloy's properties [17].

Strengthening of Inconel 718 super alloys is mainly due to γ'' precipitates. They induce a considerable coherency strain (with a tetragonal distortion $c/a=2.04$), which explains their ellipsoidal disc shape [4]. Moreover, the predominant hardening effect of the γ'' can be also explained by its higher volume fraction ($fv''/fv_{\gamma'} \approx 4$), which depends greatly on the (Ti+Al)/Nb ratio in the composition of the considered alloy [5].

It is therefore necessary to study the precipitation of the γ'' phase to better understand and predict the microstructure and mechanical behavior of Inconel 718 alloy. Since γ'' are fine and metastable particles, their quantitative characterization is not straightforward. Particle size distributions are relatively well documented thanks to extensive TEM studies [18–20]. However, particle density, volume fraction and/or solubility limits are much more difficult to characterize and very few experimental data are available [7].

The quantitative experimental data on γ'' stability (solubility product, surface energy) are rather scarce in the literature. Mons [21] has proposed a tentative TTT diagram from various literature values, which has been completed with more recent data and shown in Fig. 1. However, to the author's knowledge, no full precipitation time temperature diagram, and associated mechanical properties, is available in the literature. As it can be seen in Fig. 1, the precipitation C-curves for γ'' are rather incomplete and very scattered.

Devaux *et al.* studied the coarsening of γ'' precipitates [9] by extensive TEM image analysis and provided interesting information on the γ'' stability although in a limited temperature range. In a more recent work, Fisk *et al.* [26, 27] simulated the whole precipitation sequence of γ'' (nucleation, growth and coarsening) at 760°C using a mean radius precipitation model. They later used these data as entry parameters for the prediction of yield strength and hardening. The precipitate size distribution was post-calculated with the Lifshitz-Slyozov-Wagner (LSW) theory and accounted for by

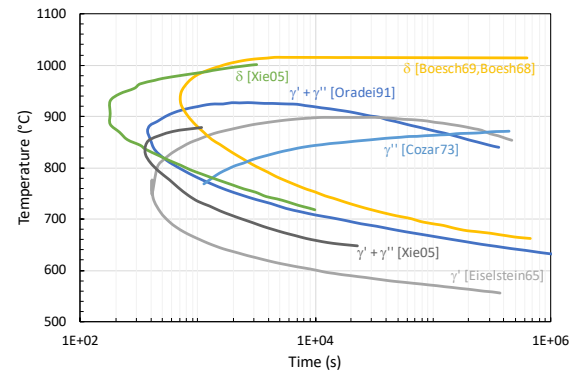


Figure 1: “Schematic” TTT diagram of 718 alloy (data from [Eiselstein65]: [22], [Xie05]: [23], [Boesch69,Boesch68]: [24, 25], [Cozar73]: [5],

weighting the fraction of sheared and bypassed precipitates. However, sheared and bypassed hardening amplitudes were estimated using a mean radius approach, which is known to be a correct estimation for isothermal treatment but fails to accurately describe non-isothermal precipitate size distribution [28–30]. More recently, Fisk *et al.* [31] completed their study and proposed a precipitation model adapted for non-isothermal treatments (*i.e.* welding), notably improving their model from a mean radius approach to an eulerian type full distribution description. Their results present a fair correlation with experimental results of the hardness in a welded joint. Furthermore, their precipitation model is only calibrated on mean radius literature data at a single temperature. A pure growth regime is observed up to 10^4 s which seems contradictory with experimental observations.

Moore *al.* [32, 33] recently proposed a model based on the Kampmann and Wagner numerical model (KWN) [34] for the precipitation of γ'' in nickel alloy 625 and 718. Their model allows to predict the shape factor of the precipitates and showed good results for the distribution of precipitates over several hours.

Matcalc simulations on alloy 718 were also proposed by Drexler *al.* [35] for the combined precipitation of γ' and γ'' . Yield stress prediction were proposed based on the hardening model developed by Ahmadi *et al.* [36]. They proposed a simulated Time Temperature Precipitate diagram (represented in Fig. 1) which is in agreement with the measured onset of strengthening over a wide range of temperatures. However, they surprisingly show simultaneous precipitation of γ' and γ'' over all studied temperatures.

Phase field simulations of the precipitation kinetics in

alloy 718 have also been performed by Zhou *et al* [37]. Although no correlation with experimental data was provided, the proposed model interestingly allows to simulate the precipitation of both γ' , γ'' and δ phases. Phase field simulations along with *ab initio* computations have also been proposed [38, 39] to describe interactions between the γ'' phase and dislocations. They detail several complex mechanisms responsible for precipitation hardening of this alloy.

Ahmadi *et al* [40, 41] have developed a model to predict the mechanical properties of precipitation hardening materials and applied it to alloy 718Plus [42]. They notably distinguish the strengthening from weak and strong shearable precipitates and were able to predict the yield limit of the aforementioned alloy for various aging times after heat treatment at 788 °C.

In summary, many studies on the precipitation kinetics and the consecutive hardening mechanisms have been proposed for the γ'' hardened alloys. However, most of these studies focus on long heat treatments, representative of the typical aging treatments and service life of the alloy for the most common aeronautical applications. Furthermore, the kinetics that would be observed during short term thermal transient, representative of manufacturing processes, such as additive manufacturing or welding have been far less studied.

In this paper, a multi-class precipitation KWN-type model is proposed. Nucleation and growth equations are adapted to disc shaped precipitates. The precipitation model is implemented in a "Lagrangian-like" model class management software (PreciSo) [28, 29, 43], which provides a distribution density of precipitates for non-isothermal heat treatments.

This model is then coupled with a yield strength model, based on the work of Bardel *et al.* [43], taking into account the whole precipitate distribution, the particular shape of the γ'' phase, their spatial distribution and the competition of two mechanisms of interactions with dislocations: bypassing and shearing. In order to describe precipitation durations more representative of manufacturing processes, experimental results are collected for times ranging from a few minutes to a few hours.

The simplicity of the proposed models allows their integration in macroscopic scale modelling, typically for processes simulation [44]. The KWN precipitation model and the mechanical model remain yet physically based and the model parameters can be linked, although not straightforwardly, to physical properties of the materials. Finally those models have proven their robustness and versatility to model various precipitation and hardening phenomena (*e.g.* fast non-isothermal treatments).

In section 2, 2.2 and 2.3, the material, associated heat treatments and characterization techniques are presented. Several precipitation states, involving mainly the presence of the γ'' phase are characterized using the Transmission Electron Microscopy (TEM) and Small Angle Neutron Scattering (SANS) techniques. In section 3, the precipitation model, source and choice of material parameters are detailed. Numerical results are confronted, for various heat treatments, with the experimental ones and data from the literature. The mechanical model and comparison with experimental results are presented in section 4. Finally, the model is discussed and simulation results for non isothermal treatments are presented.

2. Materials, heat treatments and methods

2.1. Materials

The alloy 718 bench used in this study was supplied by Safran Aircraft Engines. Its chemical composition is given in Table 1.

The base material shape is a hot forged cylinder of diameter 250 mm and height 214 mm. All samples were taken from this cylinder at constant surface distance to ensure an homogeneous initial microstructure and grain size. The as-received material was previously annealed at 955°C during 1 h and then air-cooled.

2.2. Heat treatments

Heat treatments for each characterization technique have been chosen thanks to the approximate TTT diagram taken from the literature [21] (Fig. 1). The purpose was to maximise the presence of the γ'' phase while limiting the presence of the δ and, to a lesser extent, γ' phase.

The heat treatments were all conducted in a Nabertherm furnace, in an Argon neutral atmosphere to avoid oxidation during treatment. All performed heat treatments and expected phases are listed in Table 2.

Due to the massive geometry of the as-received cylinder (250 mm diameter), a Solution Treatment (ST) (1050°C/1h) followed by water quench (WQ), was further performed on smaller samples (cylinders of 15 mm diameters for the microscopy observations and 0.5 mm thick plates for SANS) to ensure a precipitation free state before any isothermal precipitation treatment.

This solution treatment was eventually followed by a precipitation treatment performed at temperatures T during time t and water quenched. In the following, all precipitation treatments are noted T/t, as-received samples are noted AR and as-received followed by solution treatment are noted AR+ST.

	Ni	Fe	Cr	Nb	Mo	Ti	Al	Co	Si	C	Others
wt%	53.72	18.22	17.84	5.42	2.91	0.93	0.46	0.16	0.11	0.02	0.21
at%	53.16	18.95	9.93	3.39	1.76	1.13	0.99	0.16	0.23	0.10	0.22

Table 1: Chemical composition of the Inconel 718 studied alloy (as provided by Safran Aircraft Engines - material certificate).

Experimental technique	Thermal treatment	Expected phase					
		γ	MC	γ'	γ''	δ	Laves
TEM	AR+ST+760°C/1h	✓	✓	✓	✓	✗	✗
	AR+ST+760°C/2h	✓	✓	✓	✓	✗	✗
	AR+ST+720°C/2h	✓	✓	✓	✓	✗	✗
	AR+ST+720°C/4h	✓	✓	✓	✓	✗	✗
SANS	AR+ST+760°C/30min	✓	✓	✓	?	✗	✗
	AR+ST+760°C/1h	✓	✓	✓	✓	✗	✗
	AR+ST+760°C/2h	✓	✓	✓	✓	?	✗
	AR+ST+720°C/9min	✓	✓	?	?	✗	✗
	AR+ST+720°C/18min	✓	✓	✓	?	✗	✗
	AR+ST+720°C/2h	✓	✓	✓	✓	✗	✗
	AR+ST+720°C/4h	✓	✓	✓	✓	✗	✗
	AR+ST+720°C/6h	✓	✓	✓	✓	?	✗
Tensile tests	AR	✓	✓	?	?	?	✗
	ST	✓	✓	✗	✗	✗	✗
	AR+ST+760°C/1h	✓	✓	✓	✓	✗	✗
	AR+ST+760°C/2h	✓	✓	✓	✓	✗	✗
	AR+ST+720°C/1h	✓	✓	✓	✓	✗	✗
	AR+ST+720°C/1h	✓	✓	✓	✓	✗	✗
	AR+ST+720°C/2h	✓	✓	✓	✓	✗	✗
	AR+ST+720°C/4h	✓	✓	✓	✓	✗	✗
	AR+ST+720°C/7h30min	✓	✓	✓	✓	✗	✗
	AR+ST+720°C/15h15min	✓	✓	✓	✓	✗	✗

Table 2: Heat treatments for each characterization technique. AR: as received. ST: Solid Solution Treatment (1050°C/1h/WQ)

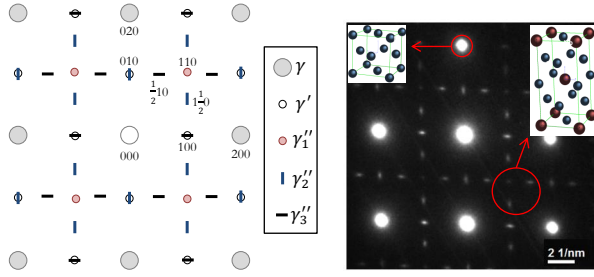


Figure 2: Right: schematic Selected Area Diffraction (SAD) patterns. [001] $_{\gamma}$ orientation. Left: experimental SAD patterns after 760°C/2h precipitation treatment (see Table 2), zone axis: [001].

2.3. Characterization techniques

In order to measure γ'' precipitates size distribution, two complementary techniques were used. Small Angle Neutron Scattering (SANS) measurements is based on the analysis of a large volume, providing statistically accurate data on precipitation radius distribution.

2.3.1. Transmission Electron Microscopy (TEM)

This technique was used to determine the γ'' phase size distribution and the shape factor $q = 2r_p/T_p$, where r_p is the radius and T_p is the thickness of the precipitate platelets. These results will be used as validation data for the precipitation modeling (see section 3). TEM characterizations were conducted on a JEOL 2010F microscope operating at 200 kV at the Consortium Lyonnais de Microscopie (CLYM) located at the University of Lyon (France).

Samples were extracted from the heat treated samples, manually polished to reach a thickness of 0.15 mm, and punched to extract usual TEM discs with a 3 mm diameter. Discs were then electro-polished in a Struers Tenupol using A2 Struers electrolyte at -15 °C, and 24.5 V.

TEM allows a differentiation between the two hardening intermetallic phases γ' and γ'' , as the diffraction spots of the two phases can clearly be distinguished when the matrix is oriented in the [001] zone axis [8, 19, 45, 46], see (Fig. 2).

With a $\langle 100 \rangle_{\gamma}$ orientation the three γ'' variants give three separate spots corresponding to the superlattice reflections at $\{100\}$, $\{110\}$ and $\{1\ 1/2\ 0\}$ positions [19]. To observe only the γ'' phase $\{1\ 1/2\ 0\}$ superlattice reflection is used, a dark field image reveals only one of the three variants. γ' particles are also observed although no evidence of co-precipitation have been found.

One example on centered $\{1\ 1/2\ 0\}$ superlattice reflection dark field for each studied heat treatment are

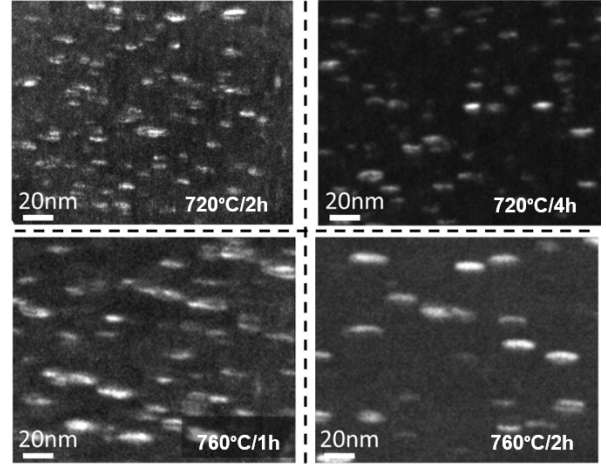


Figure 3: Dark field image using the $\{1\ 1/2\ 0\}$ superlattice reflection (see Fig. 2)

available in Fig. 3. Precipitates are homogeneously distributed in the matrix.

Dark field micrographs were used to determine the radius distributions for two temperatures at two different times. To plot these distributions, clearly visible particles on the dark field images were outlined with ImageJ software. A normalized statistical distribution is obtained, it is then multiplied by the total number of particles given by the model for each studied heat treatments. These experimental results will be represented further in section 3 and compared with modelling outputs.

2.3.2. Small-Angle Neutron Scattering (SANS)

SANS experiment were conducted at the Laboratoire Léon Brillouin (LLB) located in the Commissariat à l'Energie Atomique (CEA) Saclay. The 7 meter long SANS spectrometer Paxy was used. The samples are rectangular shaped (1 cm×1 cm×1 mm).

The detector was placed in two different configurations (see Table 3).

The neutron scattering cross section $\frac{d\Sigma}{d\Omega}(q)$ is obtained from the total integrated neutron intensity after background subtraction and normalization by the sample transmission and thickness and by the solid angle. $\frac{d\Sigma}{d\Omega}(q)$ was assumed to be the sum of 3 contributions:

$$\frac{d\Sigma}{d\Omega}(q) = I_{\text{Porod}}(q) + I_{\gamma''}(q) + I_{\text{incoherent}} \quad (2)$$

$I_{\text{Porod}}(q)$ is a $1/q^n$ signal originating from large scale scattering length fluctuations (very large particles, grain

	Configuration 1	Configuration 2
Wavelength (nm)	0.6	0.96
Sample-detector distance (m)	2	5

Table 3: SANS configurations.

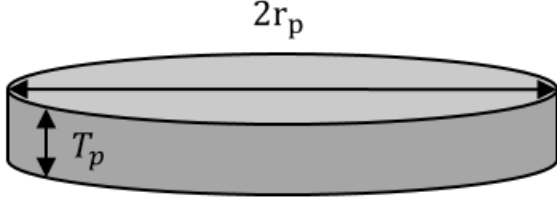


Figure 4: Disc-shaped γ'' precipitates

structure, dislocations, segregations...). $I_{\text{incoherent}}$ is a constant contribution to the signal, which originates both from the disorder in the solid solution (Laue scattering) and from the incoherent scattering of the atomic species.

$I_{\gamma''}(q)$ is modeled by the signal of an assembly of discs of radius r_p and thickness T_p (Fig. 4) with a fixed aspect ratio and with a log-normal size distribution with a dispersion parameter of 20% [47, 48]. The aspect ratio $q = 2r_p/T_p$ is assumed to follow the expression given by eq. 18 based on experimental results (more on this in section 3).

To account for the interaction between the particles, resulting in a visible maximum of intensity in some of the SANS results, we introduce a structure factor in the decoupling approximation [49] and assume that a hard-sphere model can reasonably describe the interactions between these particles. While this may be a strong assumption, the validity of the structure factor model is of low influence on the obtained particles sizes if the fit is valid in the high q range where the structure factor is close to 1.

Figure 5 shows the SANS signal obtained on samples aged at 720 °C and 760 °C for various ageing times (circles), along with the corresponding fitted intensities (solid lines).

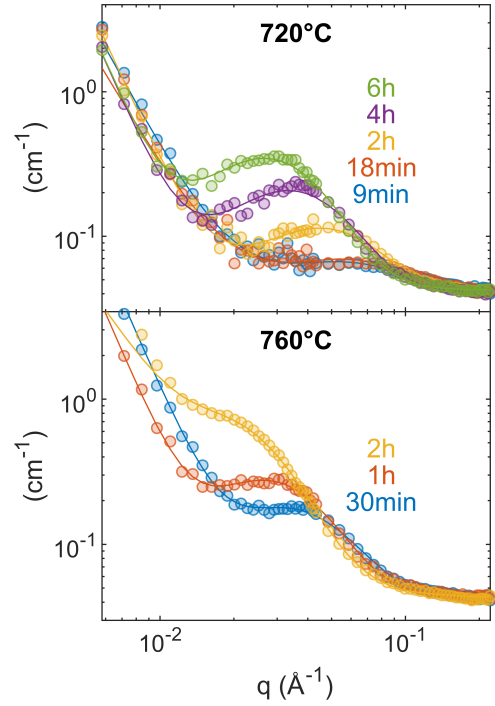


Figure 5: SANS experimental results vs fitted data for various heat treatments (circles) along with the corresponding fitted intensities (solid lines).

2.3.3. Tensile tests

Cylindrical specimens of 6 mm diameter and 40 mm length were machined from the as-received cylinder. Samples were heat treated at various times and temperatures corresponding to the microstructure characterization (see Table 2) with 6 samples at 720 °C and

4 at 760 °C. Tensile tests were carried out on a Schenck Hydraulic 250 kN system with a constant strain rate of 10^{-4}s^{-1} . During the tensile test, the strain-rate were controlled by an extensometer HZT071 for which the gauge length is 10 mm. The true strain is calculated by using the displacement measured by the extensometer. The experimental yield strengths at 0.2% strain (σ_y) are represented further in section 4 and compared with modelling outputs.

3. Precipitates modeling

3.1. KWN model with disc shaped precipitates

Classical Nucleation and Growth Theories (CNGTs) have been widely used to model the evolution of precipitate size distribution. A numerical model, originally proposed by Wagner and Kampen [50] is generally implemented for spherical precipitates [51–53]. In the case of γ'' phase in 718 alloy, this hypothesis is hardly acceptable as those precipitates exhibit platelet shapes with shape factor as large as 5-8 (see Fig. 6). It is therefore necessary to adapt the CNGT's equations to accurately model the precipitation of plate-shaped particles. The KWN model describes the evolution of the precipitate size distribution, discretized in a set of precipitates classes: at each time step, for each precipitate class i , the precipitate radius r_{p_i} and the number N_i are calculated.

This model is based on some important hypotheses:

- only the γ'' Ni_3Nb phase precipitates, whereas (γ') and δ phases are ignored. As no co-precipitation of γ'/γ'' is observed for the current alloy and under the studied conditions and although some studies suggest a role of the γ' precipitation especially in the early stages of γ'' , this effect is here neglected;
- the nucleation of γ'' in the γ matrix is homogeneous;
- γ'' precipitates are assumed to be discs (Fig. 4);
- the aspect ratio $q = 2r_p/T_p$ depends linearly on the precipitate size;
- only the niobium diffusion in the γ matrix is considered (*i.e.* nickel is massively present in the matrix and diffuses faster than niobium)

Due to the non-spherical shape of the precipitates, the energy balance of the classical nucleation theory is modified as follows.

The first step of the model is the determination of the free enthalpy (Gibbs energy) variation due to the apparition of a precipitate of volume V_p and surface S_p :

$$\Delta G = V_p \Delta g + S_p \Gamma = \frac{2\pi \Delta g}{q} r_p^3 + 2\pi \Gamma r_p^2 \left(1 + \frac{2}{q}\right) \quad (3)$$

Where Γ is the surface tension of γ'' precipitates, r_p and q are the radius and shape factor of platelets. Note that the assumption of thin-disk shaped particles instead of oblate ellipsoids does not significantly affect the external surface of the precipitates, as well as their volume (approximation within a few percents of error). The driving force Δg is calculated from the solubility product K_S of Ni_3Nb :

$$\Delta g = -\frac{k_B T}{4v_{at}^{\gamma''}} \ln \left[\frac{X_{\text{Ni}}^{\gamma} X_{\text{Nb}}^{\gamma}}{K_S} \right] \quad (4)$$

Where k_B is the Boltzmann's constant, T is the temperature, $V_{at}^{\gamma''}$ is the atomic volume of γ'' , X_{Ni}^{γ} and X_{Nb}^{γ} are the matrix atomic fraction of Ni and Nb, respectively. The solubility product is usually given by:

$$K_S = X_{\text{Ni}}^{\gamma e3} X_{\text{Nb}}^{\gamma e} = 10^{-\frac{A}{T} + B} \quad (5)$$

$X_{\text{Ni}}^{\gamma e}$ and $X_{\text{Nb}}^{\gamma e}$ are the equilibrium atomic fraction of Ni and Nb in the matrix. Parameters A and B are constants and determined experimentally.

The critical radius r_p^* above which precipitates are stable can be expressed as follow:

$$r_p^* = -\frac{2\Gamma(q+2)}{3\Delta g} \quad (6)$$

The energy barrier for nucleation ΔG^* becomes:

$$\Delta G^* = \frac{16}{3} \pi \frac{\Gamma^3}{\Delta g^2} \frac{(q+2)^3}{18q} \quad (7)$$

Note that eqs. 6 and 7 are slightly different from eqs. (22) and (23) of Fisk *et al.* [27], for which disk shape precipitates are supposed spherical when $q = 1$.

The nucleation rate is given by the CNGT:

$$\frac{dN}{dt} = N_0 \beta^* Z \exp \left[-\frac{\Delta G^*}{k_B T} \right] \left[1 - \exp \left(-\frac{t}{\tau} \right) \right] \quad (8)$$

where $N_0 = 1/v_{at}^{\gamma}$ is the nucleation site density, V_{at}^{γ} is the matrix atomic volume. The condensation rate β^* , the incubation time τ and the Zeldovitch factor Z are given by:

$$\beta^* = \frac{4\pi r_p^2}{a^4} \frac{X_{\text{Nb}}^{\gamma''}}{D_{\text{Nb}} X_{\text{Nb}}^{\gamma}} \quad (9)$$

$$\tau = \frac{2}{\pi \beta^* Z^2} \quad (10)$$

$$Z = \frac{v_{\text{at}}^{\gamma''}}{3\pi r_p^2} \sqrt{\frac{\Gamma q(q+2)}{2k_B T}} \quad (11)$$

a is the γ lattice parameter, D_{Nb} is the diffusion coefficient of Nb in the matrix, $X_{\text{Nb}}^{\gamma''} = 0.25$ is the Nb atomic fraction in the precipitate.

The growth equation for disc shaped particles has been adapted from the plate-shaped Zener-Hillert expression [54]:

$$\frac{dr_p}{dt} = \frac{q}{2} \frac{D_{\text{Nb}}}{r_p} \frac{X_{\text{Nb}}^{\gamma} - X_{\text{Nb}}^{\gamma e}(r_p)}{\alpha X_{\text{Nb}}^{\gamma''} - X_{\text{Nb}}^{\gamma e}(r_p)} \quad (12)$$

where α is the ratio of the matrix over the precipitate mean atomic volume $\alpha = v_{\text{at}}^{\gamma}/v_{\text{at}}^{\gamma''}$ and $X_{\text{Nb}}^{\gamma e}(r_p)$ is the equilibrium Nb atomic fraction in γ at the precipitate/matrix interface for a given radius r_p .

In the original Zener-Hillert equation, a multiplicative term of $1 - r_p^*/r_p$ is present to account for capillarity effects. This term is removed here because the Gibbs-Thomson effect is explicitly accounted for (see next paragraph).

To determine the equilibrium solute fractions, the influence of interfaces on equilibrium has to be taken into account: *i.e.* Gibbs-Thomson effect. The Gibbs-Thomson formalism has been adapted for disc-shaped precipitates with the method available in [51]:

$$X_{\text{Ni}}^{\gamma e 3}(r_p) X_{\text{Nb}}^{\gamma e}(r_p) = K_S \exp\left[\frac{r_{p0}}{r_p}\right] \quad (13)$$

where r_{p0} is the capillarity radius. It can be expressed as follows:

$$r_{p0} = \frac{4v_{\text{at}}^{\gamma} \Gamma 2(q+2)}{k_B T 3} \quad (14)$$

At the end of each time step, after nucleation and growth calculations, remaining Nb in the matrix can be calculated *via* a mass balance:

$$X_{\text{Nb}}^{\gamma} = \frac{X_{\text{Nb}}^0 - X_{\text{Nb}}^{\gamma''} \alpha f_v}{1 - \alpha f_v} \quad (15)$$

X_{Nb}^0 is the total atomic fraction content of element Nb and f_v is the volume fraction of γ'' precipitates. The volume fraction f_v is calculated from the precipitate distribution given by the numerical model (r_{pi} and N_i):

$$f_v = 2\pi \sum_i \frac{r_{pi}^3 N_i}{q_i} \quad (16)$$

where q_i is the aspect ratio for the precipitate class i (of radius r_{pi}).

Implementation of nucleation and growth equations (eqs. 8 and 12) has been done using PreciSo software as described in [28, 29].

3.2. Calibration of the precipitation model

γ matrix parameters. Sundararaman *et al.* [55] have measured the γ lattice parameter in Inconel 718 with the XRD method. They obtained $a = 3.616 \times 10^{-10}$ m. The matrix mean atomic volume v_{at}^{γ} can then be determined as: $v_{\text{at}}^{\gamma} = a^3/4 = 1.182 \times 10^{-29}$ m³.

Niobium diffusion parameters. The evolution of niobium diffusion coefficient is classically described by an Arrhenius law:

$$D_{\text{Nb}} = D_{\text{Nb}}^0 \exp\left[-\frac{Q}{RT}\right] \quad (17)$$

Pavil *et al.* [56] or Karunaratne *et al.* [57] have proposed diffusion coefficients of niobium in pure nickel which are not necessarily valid for highly alloyed materials such as Inconel 718 [58]. Following the example of Devaux *et al.* [9] and Low *et al.* [59] the pre-exponential factor D_{Nb}^0 has been fixed to 8.8×10^{-5} m²·s⁻¹. The activation energy Q has been found equal to 272 kJ·mol⁻¹ by Devaux *et al.* [9] and 286 kJ·mol⁻¹ by Han *et al.* [60] for respective niobium weight fractions of 5.3% and 4.94%. Here, and in a similar way to Low *et al.* [59], Q was taken as 263 kJ⁻¹ for a niobium weight fraction of 5.42%.

γ'' precipitate parameters. The composition of γ'' precipitates has been measured by Miller *et al.* [61] using Atom Probe Tomography: they found 74 at% Ni, 17 at% Nb among many other elements. For the sake of simplicity, the stoichiometric binary Ni₃Nb composition is used here. The γ'' lattice parameters have been reported by Wagner and Hall [50], the resulting mean atomic volume is $v_{\text{at}}^{\gamma''} = 1.157 \times 10^{-29}$ m³.

Devaux *et al.* [9] calculated the γ/γ'' interfacial energy as $\Gamma = (95 \pm 17)$ mJ/m². Here, a value of 100 mJ/m², consistent with Devaux's calculation was chosen.

A comparison between the experimental aspect ratio versus mean radius evolution obtained in this study and the literature data is presented in Fig.6. TEM measured aspect ratios are in agreement with the literature

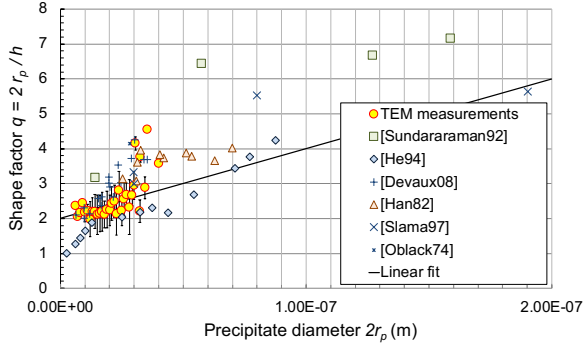


Figure 6: aspect ratio vs precipitate diameter. TEM results compared with literature data

results. A large discrepancy of values is observed from the different sources, certainly due to the large period of time over which data were collected (and associated progresses in measurement techniques). For the sake of simplicity a simple linear fit describing the evolution of the aspect ratio with the precipitate radius has been implemented in the model:

$$q = 2 \times 10^7 \text{ m}^{-1} \times 2r_p + 2 \quad (18)$$

In this approach, the precipitate aspect ratio q is updated according to eq. 18 after each time step.

Various literature studies have proposed measurements of niobium concentration in Inconel 718 matrix at equilibrium [9, 35, 62, 63] with a rather large discrepancy. Fisk *et al.* [31] have proposed a temperature dependant relation for the equilibrium concentration of niobium in their precipitation model. The solubility product of the γ'' phase is therefore classically described as the following equation, consistent with the literature data and the temperature dependency proposed by Fisk *et al.* [31].

$$\log_{10}(Ks) = -\frac{A}{T} + B \quad (19)$$

with $A=3294 \text{ K}$ and $B=0.3997$.

All precipitation model parameters are listed in Table 4.

3.3. Precipitation simulation: results and discussion

From an initial supersaturated solid solution, three isothermal precipitation treatments have been modeled at 660, 720 and 760 °C. Figure 7 shows the comparison between predicted and experimental mean radii evolution with time. Predicted values of precipitate radius show the classical growth ($\propto t^{1/2}$) and coarsening ($\propto t^{1/3}$) regimes. It can be noticed that increasing

Parameter	Value	Ref.
$a \text{ (m)}$	3.616×10^{-10}	[55]
$v_{at}^\gamma \text{ (m}^3\text{)}$	1.182×10^{-29}	[55]
$D_{Nb}^0 \text{ (m}^2\text{/s)}$	8.8×10^{-5}	[57], [9]
$Q \text{ (kJ/mol)}$	263	[9], [60], [59]
$v_{at}^{\gamma''} \text{ (m}^3\text{)}$	1.157×10^{-29}	[50]
$\Gamma \text{ (mJ/m}^2\text{)}$	100	[9]
$A \text{ (K)}$	3294	[31], this work
B	0.3997	[9, 31, 35, 62, 63], this work

Table 4: Precipitation model input parameter synthesis

temperature accelerates the precipitation kinetics as the three investigated temperatures range in the diffusion limited domain (lower part of the C-curve).

For the three investigated temperatures, simulated radii are in good agreement with SANS and TEM measurements, as well as other experimental data from the literature. The model predicts a growth to coarsening transition at approximately 100 s for the three studied temperatures and almost all experimental values fall in the coarsening regime, as in the study of Fisk *et al.*, for which a mean radius model [27] is used. However, in a more recent paper, Fisk *et al.* used a more elaborate precipitation model (KWN-type) [31] that is compared with data only in the pure growth regime (below $2 \times 10^4 \text{ s}$) with another set of simulation parameters at 750 °C only.

The volume fraction and number density of precipitates as a function of time are given in Fig. 8 for the three investigated temperatures: 660, 720 and 760 °C. Note that the final precipitate volume fraction at 760 °C is approx. 9%, whereas Fisk *et al.* [27, 31] find a value of 12% at 760 °C and Drexler *et al.* [35] a value of $\approx 10\%$ at 720 °C and 11% at 620 °C. There is however a larger disagreement on the characteristic precipitation time t_{50} (time to precipitate 50% of the maximum volume fraction), for which we find 50 s and Fisk *et al.* find 1000 s at 760 °C. However, Drexler *et al.* found a t_{50} of about 700 s at 800 °C, which is in good agreement with the 400 s from our model. Note that the precipitation time is extremely sensitive to temperature in the upper part of the C-curve (above 750 °C), as shown in the TTT diagram presented later on.

Experimental precipitate distributions were obtained from TEM. They are compared with modeled distributions in Fig. 9, where a general agreement can be observed. Experimental distributions exhibit a tail for large precipitates that is not predicted by the precipitation model. The model also predicts more small precipitates. The experimental size distribution has a

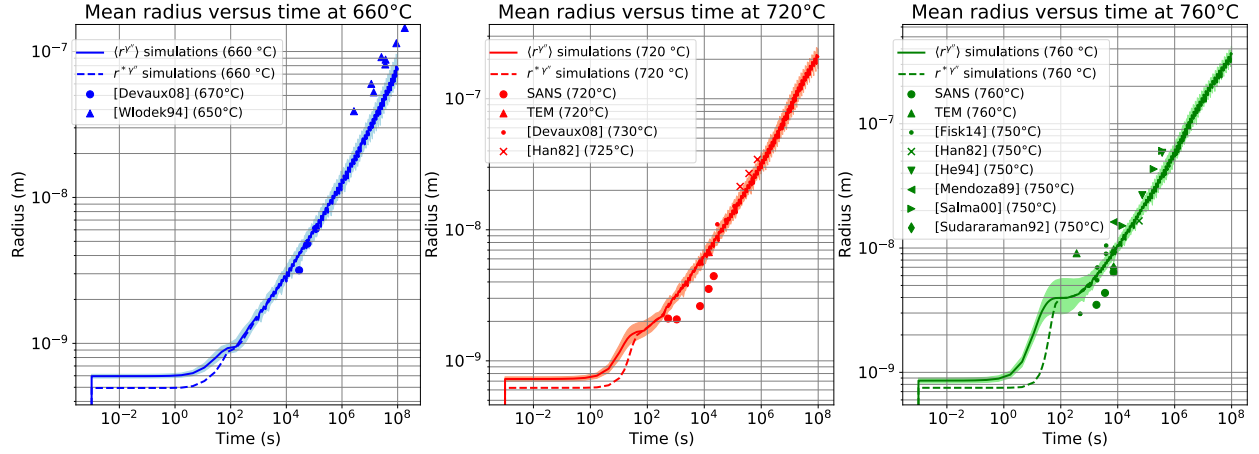


Figure 7: Mean radius as a function of time for different treatment temperatures. Simulation versus experimental data (shaded colors represent simulation results at $\pm 10^\circ\text{C}$).

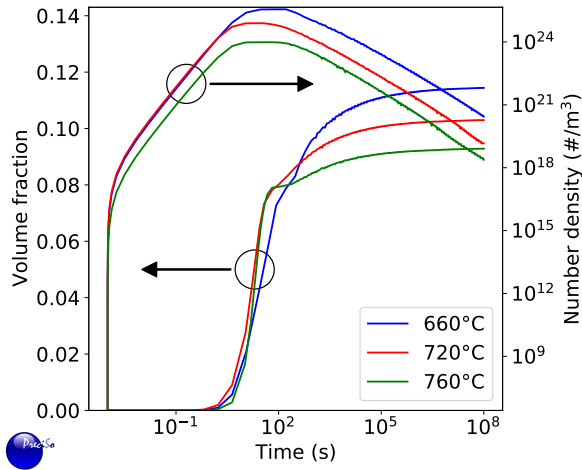


Figure 8: Simulated volume fraction and number of precipitates versus of time and treatment temperature.

log-normal shape, whereas the simulation has a LSW shape. These differences are classically observed and have rarely been explained (see ref. [64]). Some possible causes of are: (i) small precipitates are not seen by TEM; (ii) large precipitates seen by TEM may be the results of diffusion short-circuits not accounted for in the precipitation model; (iii) LSW shape is based on the non-impingement of diffusion fields, which may not be the case at high precipitate volume fraction.

4. Yield strength estimation

4.1. Yield strength model: presentation and calibration

In this section a model based on the interaction between dislocations and defects is proposed in order to calculate the yield strength. The influence of the γ' precipitates, not modelled in this study, on the mechanical properties is neglected as currently assumed in the literature. The classical formulation, originally proposed by Friedel [65], and improved by Kocks *et al.* [66] and Deschamps *et al.* [67] is used to take into account the precipitation state:

$$\sigma_y = \sigma_0 + \Delta\sigma_{SS} + \Delta\sigma_p \quad (20)$$

where σ_0 is the yield strength of the base material. It includes Peierls-Nabarro stress, the forest dislocation contribution, the Hall-Petch effect, and the solid solution strengthening of alloying elements, except *Nb*. This contribution is supposed constant during all heat treatments since the initial solution treatment anneals the dislocations and leads to a relatively large grain size

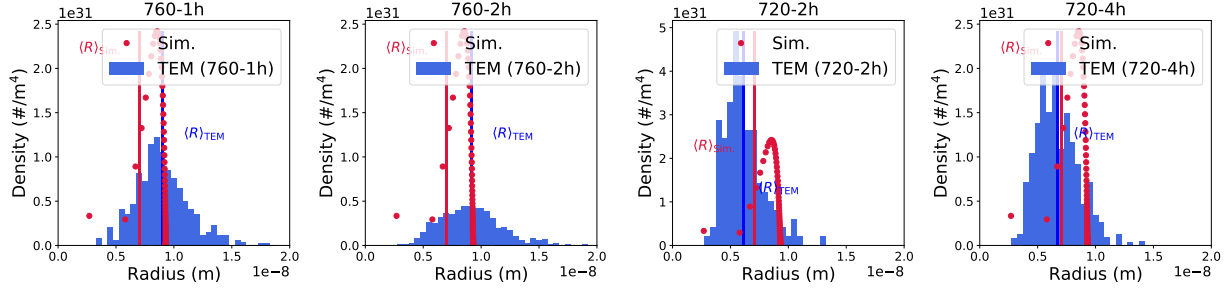


Figure 9: Precipitate radius distribution: simulation vs experimental data from TEM.

that therefore slightly changes during subsequent treatments. $\Delta\sigma_{SS}$ and $\Delta\sigma_p$ are the contributions of Nb in solid solution and γ'' precipitates, respectively. These two contributions are linearly summed up according to Kocks *et al.* [66].

4.1.1. Solute niobium content contribution $\Delta\sigma_{SS}^{Nb}$

Mishima *et al.* [68] studied the effect of various solute elements in Nickel alloys on yield strength. They proposed the following relation:

$$\Delta\sigma_{SS}^{Nb} = A_{Nb} \sqrt{X_{Nb}^{\gamma}} \quad (21)$$

where X_{Nb}^{γ} is the Nb atomic concentration (in at%) and $A_{Nb} = 1.17 \times 10^9 \text{ Pa}\cdot\text{at}\%^{-0.5}$ is a constant.

4.1.2. Constant contribution σ_0

To determine the yield strength of the base material, the annealed sample yield strength (treatment AR+ST, see 2) is used. In this precipitate free sample, $\sigma_y = \sigma_0 + \Delta\sigma_{SS}^{Nb} = 352 \text{ MPa}$. From the Nb content of the alloy and using eq. 21, the constant contribution σ_0 is estimated at 137 MPa.

4.1.3. Precipitation hardening $\Delta\sigma_p$

The precipitate hardening can be written as follows [66, 67]:

$$\Delta\sigma_p = \frac{M\bar{F}}{b\bar{L}} = \frac{M}{b\bar{L}} \frac{\sum_i N_i(r_{pi}) F_i(r_{pi})}{\sum_i N_i(r_{pi})} \quad (22)$$

where \bar{F} is the mean obstacle strength and \bar{L} is the mean particle spacing. To take into account the whole γ'' radius distribution, the summation of each precipitate class i contribution is performed using $N_i(r_{pi})$, the number density of precipitates of radius r_{pi} and $F_i(r_{pi})$ the force acting on precipitates of radius r_{pi} .

Depending on their radius, precipitates can be either sheared (small precipitates) or bypassed (large ones).

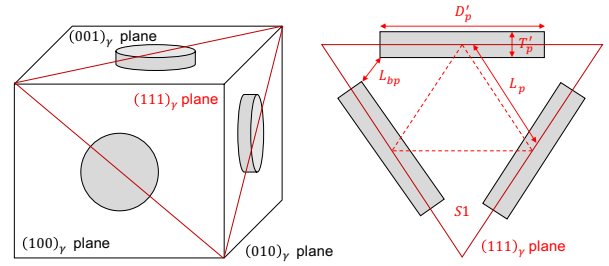


Figure 10: Disposition of plate precipitates in the slip plane

Bypassed precipitates. For bypassed precipitate class i , the force acting on the dislocation is:

$$F_i^{bp}(r_{pi}) = 2\beta G b^2 \quad (23)$$

where β is a constant parameter usually assumed to be equal to 0.5 ([67, 69]). However, according to Brown *et al.* [70], $\beta = 0.25$ is a more realistic value, which will be used here.

The mean particle spacing is a key parameter. It strongly depends on the precipitate density, orientation and shape. For precipitate plates oriented in the $\{100\}_\gamma$ and $\{111\}_\gamma$ slip planes, Nie *et al.* [71] proposed a relation between the distance between particle centres L_p and the space left for the dislocation to bypass precipitates L_{bp} (see Fig. 10):

$$L_{bp} = L_p - \frac{D'_p}{2} - \frac{\sqrt{3}}{2} T'_p \quad (24)$$

where D'_p and T'_p are the mean bypassed precipitate diameter and thickness as seen by the dislocation moving in the slip plane (see Fig. 10). Thickness T'_p is related to the precipitate thickness through the angle θ between $\{100\}_\gamma$ and $\{111\}_{\gamma'}$ ($\cos \theta = 1/\sqrt{3}$):

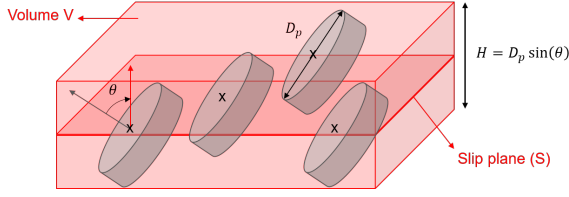


Figure 11: Intersection of the slip plane with plates of diameter D_p in the parallelepiped of thickness H

$$T'_p = \frac{T_p}{\sin \theta} = T_p \sqrt{\frac{3}{2}} = \frac{3}{\sqrt{2}} \frac{\sum_{i>i_c} N_i r_{pi} \frac{r_{pi}}{q_i}}{\sum_{i>i_c} N_i} \quad (25)$$

where r_{pi} , N_i and q_i are the radius, the number and aspect ratio of precipitate class i , and i_c is the critical precipitate class at which the dislocation changes from shear to bypass mechanism.

The average intersect diameter of a plate of diameter D_p intersecting a given plane is $\pi D_p/4$. The mean diameter D'_p is then given by:

$$D'_p = \frac{\pi D_p}{4} = \frac{\pi}{2} \frac{\sum_{i>i_c} N_i r_{pi}}{\sum_{i>i_c} N_i} \quad (26)$$

To determine the distance L_p between particles centres, the number of precipitates per unit area in the slip plane N_a is determined in two different ways. First, Fig. 10 shows that $3/2$ precipitates are lying in the equilateral triangle of surface $L_p^2 \sqrt{3}$, leading to:

$$N_a = \frac{\sqrt{3}}{2L_p^2} \quad (27)$$

Then, N_a can be estimated considering the number of particles intersecting a plane of unit surface. The centre of these particles is located within a parallelepiped of thickness $D_p \sin \theta$ (see Fig. 11). The number of precipitates per unit area is then related to the number of precipitates per unit volume N_v via:

$$N_a = N_v D_p \sin \theta = N_v D_p \sqrt{\frac{2}{3}} = \sqrt{\frac{8}{3}} \sum_{i>i_c} N_i r_{pi} \quad (28)$$

with N_v the number of precipitates per unit volume.

The distance L_p can then be expressed as:

$$L_p = \sqrt{\frac{3}{4 \sqrt{2} \sum_{i>i_c} N_i r_{pi}}} \quad (29)$$

Finally, using eqs. 24, 25, 26 and 29, L_{bp} can be expressed with the precipitation model outputs:

$$L_{bp} = \sqrt{\frac{3}{4 \sqrt{2} \sum_{i>i_c} N_i r_{pi}}} - \frac{\pi}{4} \frac{\sum_{i>i_c} N_i r_{pi}}{\sum_{i>i_c} N_i} - \frac{3}{\sqrt{2}} \frac{\sum_{i>i_c} N_i \frac{r_{pi}}{q_i}}{\sum_{i>i_c} N_i} \quad (30)$$

Sheared precipitates. For sheared precipitates, Friedel's approach [65] is modified to account for non-spherical precipitates. The intersection surface between precipitates and the slip plane is assumed to be a rectangle of surface $D'_p T'_p$ (see Fig. 10). A disc of radius r_p^{eq} and equivalent surface is considered, leading to:

$$r_p^{eq} = \sqrt{\frac{D'_p T'_p}{\pi}} = \left(\frac{3}{2}\right)^{\frac{1}{4}} \frac{r_p}{\sqrt{q}} \quad (31)$$

The force acting on the sheared precipitates of mean intercept radius \bar{r} is given by:

$$F_i^{sh} = kGb\bar{r} \quad (32)$$

The constant term k that drives the shear force is commonly derived from the critical radius r_c , assuming that for a precipitate of equivalent radius r_c , shearing and bypassing forces acting on the precipitate are equal. Chaturvedi *et al.* determined this transition radius as $r_c = 12$ nm through creep tests [6] and this value is commonly used in the literature [26, 31]. It is also consistent with the TEM observation (Fig. 3). This would lead to a value of k close to 0.015. The constant term k could also been determined from refs. [4]. In this study, the antiphase boundary energy $\Gamma_{\gamma''} = kGb/2 = 296$ mJ/m² was measured, leading to $k = 0.029$. By adjustment with the yield stress experimental results and consistently with the literature, the value of k was finally chosen equal to 0.02.

Accounting for the averaged sheared surface of plates, for the orientation of the shear plane and assuming that the force only depends on the sheared surface, the average force acting on the dislocation is then:

$$F^{sh} = \frac{\sum_{i<i_c} N_i F_i^{sh}}{\sum_{i<i_c} N_i} = kGb \left(\frac{3}{2}\right)^{\frac{1}{4}} \frac{\sum_{i<i_c} N_i r_{pi} q_i^{-0.5}}{\sum_{i<i_c} N_i} \quad (33)$$

If precipitates are sheared, the distance L_{sh} between obstacles that interact with the dislocation line depends on the radius of curvature of the dislocation, which depends itself on the applied stress. The argument of Friedel [65] is that, on average the area A swept by the dislocation after breaking free of an obstacle contains

exactly one obstacle, so $AN_a = 1$. The area A can be estimated from geometrical considerations (see ref. [72] for calculation detail). The former consideration leads to an estimation of the spacing of precipitates centres.

The average force acting on the dislocation is then:

$$L_{sh} = \sqrt{\frac{4\Gamma_l}{\sqrt{3}}} F^{sh-0.5} L_p$$

$$= F^{sh-0.5} \sqrt{\frac{\Gamma_l \sqrt{3}}{\sqrt{2}}} \left(\sum_{i < r_c} N_i r_{pi} \right)^{-0.5} \quad (34)$$

with Γ_l the line tension $\Gamma_l = \beta G b^2$.

Summary. For bypassed precipitates:

$$\Delta\sigma_p^{bp} = 2M\beta G b \left[\sqrt{\frac{3}{4\sqrt{2} \sum_{i > r_c} N_i r_{pi}}} - \frac{\pi \sum_{i > r_c} N_i r_{pi}}{4 \sum_{i > r_c} N_i} - \frac{3 \sum_{i > r_c} N_i \frac{r_{pi}}{q_i}}{\sqrt{2} \sum_{i > r_c} N_i} \right]^{-1} \quad (35)$$

For sheared precipitates:

$$\Delta\sigma_p^{sh} = M(kG)^{\frac{3}{2}} \left(\frac{3}{2} \right)^{\frac{1}{8}} \sqrt{\frac{b}{\Gamma_l}} \left(\sum_{i < r_c} N_i r_{pi} \right)^{-0.5}$$

$$\left[\frac{\sum_{i < r_c} N_i r_{pi} q_i^{-0.5}}{\sum_{i < r_c} N_i} \right]^{\frac{3}{2}} \quad (36)$$

The precipitate shearing and bypassing contributions are added according to a quadratic summation law as in refs. [67] and [66], although other authors (see e.g. [31]) use a linear summation. The result is then put into eq. (20) to obtain the overall yield strength.

The input parameters for the yield strength model are summarized in Table 5.

4.2. Yield strength estimation results and discussion

The comparison between experimental and simulated yield strength is shown in Fig. 12 for precipitation treatments performed at 660, 720 and 760 °C. The point at 0 s holding time corresponds to the AR+ST treatment (solid solution).

The experimental yield strength was determined from tensile tests and error bars corresponds to twice the standard deviation. The predicted values of tensile strength are in very good agreement with the experimental data for 720 °C and 760 °C.

Parameter	Value	Source
σ_0 (MPa)	137	This study
M	3.06	[67, 73–75]
G (GPa)	80	[76]
b (m)	2.54×10^{-10}	[4]
A_{Nb} (MPa.at $^{0.5}$)	1170	[68]
β	0.25	[70]
r_c (nm)	12	[6]
k	0.02	[4, 6]

Table 5: Yield strength model input parameters

Figure 12 shows all contributions of hardening (eq. (20)). The contribution of niobium solute atoms decreases from 215 MPa to 120 MPa for 720 °C and to 146 MPa for 760 °C as precipitation occurs (see Fig. 8).

The precipitate hardening contributions $\Delta\sigma_p^{bp}$ and $\Delta\sigma_p^{sh}$ depend on precipitate size distributions. The bypassed precipitates contribution remains zero until the largest precipitate class reaches the critical radius r_c . At this moment $\Delta\sigma_p^{sh}$ reaches its maximum value and decreases until most precipitate size classes exceed r_c , leading to a negligible contribution of sheared precipitates $\Delta\sigma_p^{sh}$. The maximum total yield strength occurs when the mean radius reaches r_c , as usually observed for structural hardening alloy with sheared and bypassed precipitates.

This coupled approach between a multi-class precipitation model and a hardening model provides a remarkable agreement in the final yield strength prediction. Note that the precipitation model output (precipitate size distribution) has been checked and validated independently by TEM and SANS observations.

The whole precipitate size distribution contributes to the structural hardening because the average distance between precipitates directly depends on precipitates number density, which itself is not satisfactory described by a mean radius precipitation model (see [28, 29]).

The yield strength model presented in this section is a simplification of the true physical phenomenon acting in the alloy 718. Indeed, Oblak *et al.* [4, 77] observed that shearing of γ'' precipitates was possible only considering doublets or quadruplets of dislocations. They proposed a model, based on the mechanical equilibrium of two (or four) interacting dislocations shearing γ'' precipitates. Unfortunately, this model leads to a lower hardening with a quadruplet than with one single dislocation, which is not satisfactory to explain the very good resistance of γ'' precipitates. Later, Sundararaman *et al.* [78] completed this model but again the

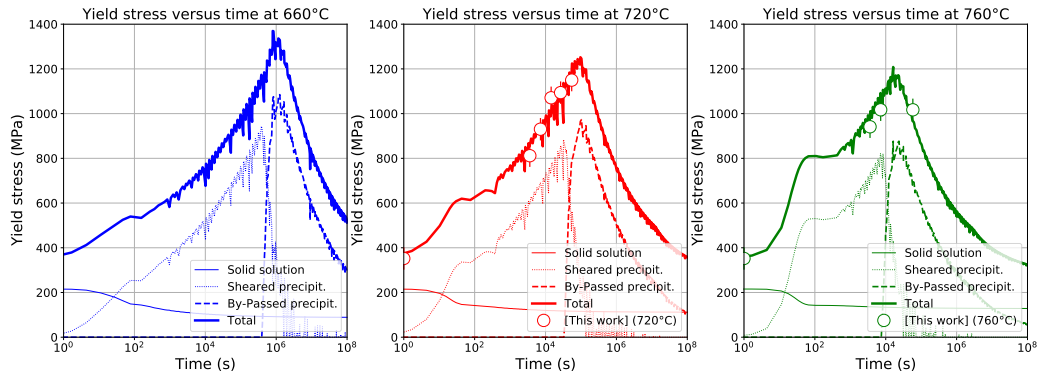


Figure 12: Yield strength in function of holding time: simulation versus experimental data

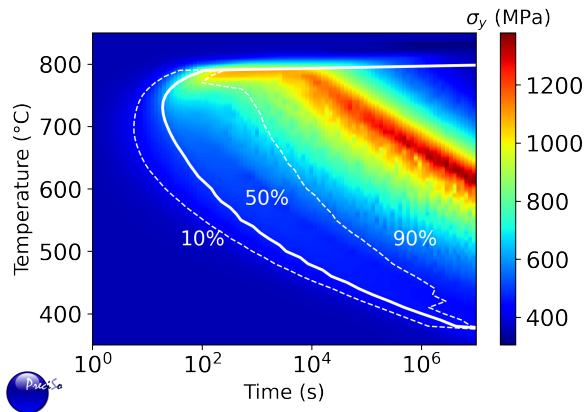


Figure 13: TTT diagram coupled with yield strength model. The model shows that although precipitation is rather fast, the hardening peak is obtained after relatively long treatment.

shear strength for four dislocations was found smaller than for the crossing of one single dislocation. In this study a "classical" single dislocation model was considered with an antiphase boundary energy of the γ'' phase equal to the value measured by [77] and used by [55] and [78]. More sophisticated approaches have been recently proposed by Ahmadi *et al.* [36, 40–42]. However, they lead to similar results, justifying thus the use of our simpler approach.

The precipitation and yield strength models used to plot the TTT diagram for γ'' precipitation reaction, superimposed with the evolution of yield stress. This diagram is presented in Fig. 13.

From this TTT diagram, we can see a much faster precipitation compared to previous TTT diagrams (see figure 1). However, considering the yield strength val-

ues represented at every point of this diagram, it can be observed that the maximal yield strength is reached much later than the precipitation equilibrium volume fraction, apart from temperatures near 780 °C, for which the δ phase is expected to replace γ'' . For most temperatures, the yield strength reaches its maximal value for isothermal treatments between 3 h and 3000 h. The apparent contradiction with previous literature data on precipitation kinetics can now be explained. The numerous small precipitates appearing quickly are very weak obstacles to the dislocations displacement, which explains the weak hardening despite the important precipitation. Precipitates growth (by coarsening) is then necessary to reach the maximum hardening. Moreover, recent experiments and simulations performed by Drexler *et al* [35] confirm this relatively fast (and weak) precipitation.

The yield strength prediction on this diagram is in good agreement with experimental observations of relatively slow hardening for this alloy. The 718 alloy is indeed known to be an alloy with a slow hardening behavior compared to others nickel based superalloys hardened by the γ' phase [2].

Industrial hardening treatments typically involve a 8 to 10 h holding between 720 and 760 °C from a super saturated solid solution state, which is in agreement with the TTT diagram. Moreover, Ahmadi *et al.* [36] reach a maximum yield stress after 25 hours at 718 °C, which exactly corresponds to the hardening peak at this temperature in Fig. 13.

5. Non-isothermal prediction of precipitation and yield strength

The knowledge of the precipitate size distribution is also needed to account for non-isothermal treatments as

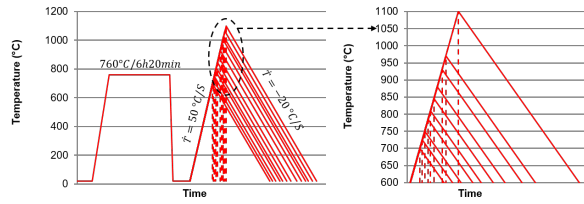


Figure 14: Non-isothermal treatments tested: heating rate of 50 °C up to variable maximum temperature T_{Max} , followed by (i) 20 °C (full line) and, (ii) instantaneous cooling (dashed line).

shown in refs [29, 29, 30]. In this section, the coupled microstructural and yield strength predictions are tested on non-isothermal treatments, which are representative of welding or additive manufacturing processes at various points of the heat affected zone.

From a super saturated solid solution, a precipitation treatment at 760 °C during 6 h 20 min is performed followed by a quick cooling (water quench) (*i.e.* corresponding to the hardness peak). After that, various non-isothermal thermal transients are tested. First a constant heating rate of 50 °C·s⁻¹ is applied up to variable maximum temperature T_{Max} . Two different cooling rates are then applied: 20 °C·s⁻¹ and instantaneous cooling to freeze the microstructure (that would correspond to a water quench). Maximal reached temperatures T_{Max} lie between 700 and 1100 °C. The studied heat treatments are presented in Fig. 14.

At the initial state of peak hardness, the precipitate volume fraction is maximum and equal to 11% with a mean radius close to 14 nm. For heat treatments up to 800 °C this state remains unchanged as the time and temperature are too low to induce any change. Above this temperature, volume fraction and precipitate radius drop as the precipitates start to dissolve. From a maximum temperature of roughly 1000 °C all precipitates have been dissolved at T_{Max} . After water quench, no precipitate remains. After cooling at 20 °C·s⁻¹, nucleation of small precipitates occurs during cooling, leading to a volume fraction of 2%.

Concerning mechanical properties, the initial state represents the hardening peak, essentially due to precipitate strengthening by bypass mechanism. As for the microstructure, nothing occurs until a maximal temperature of 800 °C. Then, a drop of mechanical properties, associated to precipitates shrinkage, is observed. For T_{Max} ranging between 800 °C and 1000 °C, followed by a water quench, the shearing contribution increases as precipitates shrink. Above a reached temperature of 1000 °C only the solid solution hardening remains

as precipitates are fully dissolved. When the heating is followed by a slow cooling, the material remains at high temperature for a longer time and therefore precipitates continue to shrink for a while, leading to a lower precipitate contribution to the overall yield limit. This phenomenon is in competition with the nucleation that occurs during cooling at lower temperatures. However the effect of this secondary precipitation is quite limited (around 100 MPa).

From the non affected zone to the most affected zone (for T_{Max} temperatures larger than 1000 °C), the yield stress drops from 1300 MPa to approx. 450 MPa (200 MPa for the solid solution $\Delta\sigma_{SS}^{Nb}$ and 150 MPa for the small secondary sheared precipitates contributions respectively).

6. Conclusion

A coupled precipitation and yield strength model was developed to describe the microstructural and strengthening evolution occurring during any heat treatment of a 718 Ni based alloy.

A recently developed precipitation model was improved to account for plate-shaped particles. This model gives the particle size distribution, later used as input data for the prediction of the yield strength. The precipitation model was calibrated by SANS and TEM analyses on isothermally treated samples.

All parameters of the coupled models were taken from the literature or experimentally determined. An excellent estimation of the yield strength was obtained by the coupled approach for isothermal treatments. The TTT diagram, coupled with the yield strength model, illustrates the slow structural hardening of the 718 alloy despite the fast precipitation of the γ'' phase.

Non-isothermal treatments, representative of different positions around a weld joint or for any point of part built by additive manufacturing, have been simulated. It has been observed that the yield strength strongly depends on the competition between the dissolution of the precipitates presents before the welding and the nucleation of new precipitates during the cooling.

7. Acknowledgements

The Consortium Lyonnais de Microscopie (CLYM) is gratefully acknowledge for the access to the 2010F microscope. Thanks are also due to the Laboratoire Léon Brillouin (LLB) at the French Atomic Energy Commission (CEA), Saclay for providing SANS beamtime. The authors would like to acknowledge the

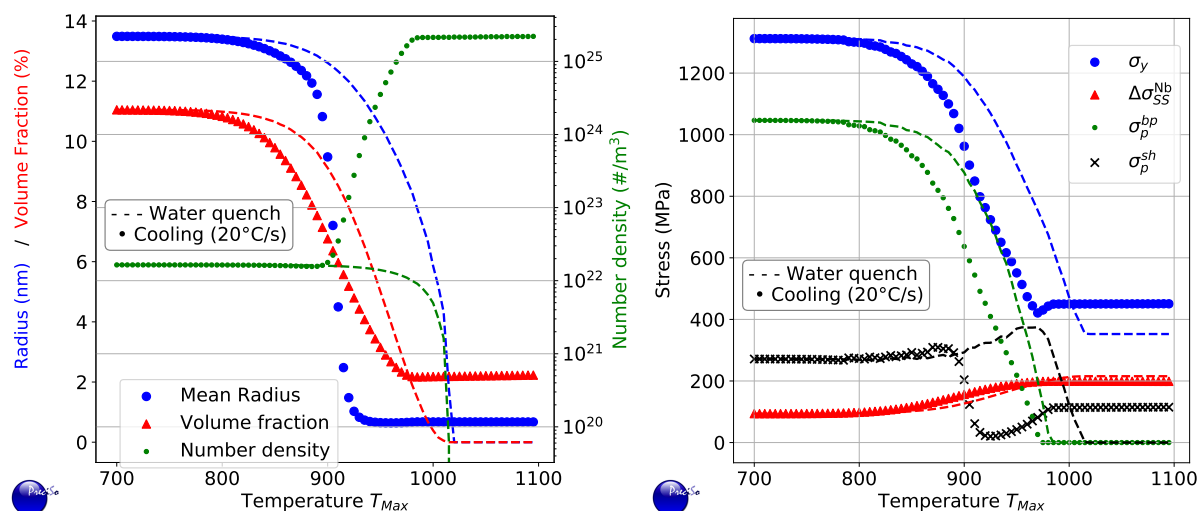


Figure 15: Microstructural and yield strength prediction for non-isothermal treatments

AREVA-SAFRAN "Life extension and manufacturing processes" chair for the financial support. Florian Mercier and Philippe Chaudet are greatly acknowledged for technical support. Many thanks to Marie-Hélène Mathon for providing the access to LLB and helping with the experiments.

8. Bibliography

References

- [1] R. C. Reed. *The superalloys: fundamentals and applications*. Cambridge university press, 2008.
- [2] A. Lingenfelter. Welding of inconel alloy 718: A historical overview. In E.A. Loria, editor, *Superalloy 718 - Metallurgy and Applications*, volume 718, pages 673–683. The Minerals, Metals & Materials Society, 1989.
- [3] D.F. Paulonis, J.M. Oblak, and D.S. Duvall. Precipitation in nickel-base alloy 718. Technical report, Pratt and Whitney Aircraft, Middletown, Conn., 1969.
- [4] J.M. Oblak, D.F. Paulonis, and D.S. Duvall. Coherency strengthening in ni base alloys hardened by do 22 γ' precipitates. *Metallurgical Transactions*, 5(1):143, 1974.
- [5] R. Cozar and A. Pineau. Morphology of γ' and γ'' precipitates and thermal stability of inconel 718 type alloys. *Metallurgical Transactions*, 4(1):47–59, 1973.
- [6] M.C. Chaturvedi and Y. Han. Effect of particle size on the creep rate of superalloy inconel 718. *Materials Science and Engineering*, 89:L7–L10, 1987.
- [7] J. He, S. Fukuyama, and K. Yokogawa. γ'' precipitate in inconel 718. *Journal of Materials Science and Technology*, 10(4):293–303, 1994.
- [8] M. Gao, D. G. Harlow, R. P. Wei, and S. Chen. Preferential coarsening of γ'' precipitates in inconel 718 during creep. *Metallurgical and Materials Transactions A*, 27(11):3391–3398, 1996.
- [9] A. Devaux, L. Nazé, R. Molins, A. Pineau, A. Organista, J.Y. Guédou, J.F. Uginet, and P. Héritier. Gamma double prime precipitation kinetic in alloy 718. *Materials Science and Engineering: A*, 486(1-2):117–122, 2008.
- [10] Y. Tian, D. McAllister, H. Colijn, M. Mills, D. Farson, M. Nordin, and S. Babu. Rationalization of Microstructure Heterogeneity in INCONEL 718 Builds Made by the Direct Laser Additive Manufacturing Process. *Metallurgical and Materials Transactions A*, 45(10):4470–4483, 2014.
- [11] V. Kindrachuk, N. Wanderka, and J. Banhart. γ'/γ'' Coprecipitation in Inconel 706 alloy: A 3D finite element study. *Materials Science and Engineering: A*, 417(1-2):82–89, 2006.
- [12] P. J. Phillips, D. McAllister, Y. Gao, D. Lv, R. E. A. Williams, B. Peterson, Y. Wang, and M. J. Mills. Nano γ'/γ'' composite precipitates in Alloy 718. *Applied Physics Letters*, 100(21):211913, 2012.
- [13] R. Shi, D. P. McAllister, N. Zhou, A. J. Detor, R. DiDomizio, M. J. Mills, and Y. Wang. Growth behavior of γ'/γ'' coprecipitates in Ni-Base superalloys. *Acta Materialia*, 164:220–236, 2019.
- [14] A. J. Detor, R. DiDomizio, R. Sharghi-Moshtaghin, N. Zhou, R. Shi, Y. Wang, D. P. McAllister, and M. J. Mills. Enabling Large Superalloy Parts Using Compact Coprecipitation of γ' and γ'' . *Metallurgical and Materials Transactions A*, 49(3):708–717, 2018.
- [15] F. Theska, A. Stanojevic, B. Oberwinkler, S.P. Ringer, and S. Primig. On conventional versus direct ageing of Alloy 718. *Acta Materialia*, 156:116–124, 2018.
- [16] F. Theska, K. Nomoto, F. Godor, B. Oberwinkler, A. Stanojevic, S.P. Ringer, and S. Primig. On the early stages of precipitation during direct ageing of Alloy 718. *Acta Materialia*, 188:492–503, 2020.
- [17] F. Theska, A. Stanojevic, B. Oberwinkler, and S. Primig. Microstructure-property relationships in directly aged Alloy 718 turbine disks. *Materials Science and Engineering: A*, 776:138967, 2020.
- [18] D. Jianxin, X. Xishan, and Z. Shouhua. Coarsening behavior of γ'' precipitates in modified inconel 718 superalloy. *Scripta Metallurgica et materialia*, 33(12):1933–1940, 1995.

- [19] M. Sundararaman, P. Mukhopadhyay, and S. Banerjee. Some aspects of the precipitation of metastable intermetallic phases in inconel 718. *Metallurgical Transactions A*, 23(7):2015–2028, 1992.
- [20] J.D. Boyd and R. Nicholson. The coarsening behaviour of θ'' and θ' precipitates in two al-cu alloys. *Acta Metallurgica*, 19(12):1379–1391, 1971.
- [21] C. Mons. Traitements thermiques des superalliages. *Techniques de l'ingénieur Traitements thermiques des aciers, des alliages et des fontes*, TIB364DUO.(m1165), 1996.
- [22] H. Eiselstein. Metallurgy of a columbium-hardened nickel-chromium-iron alloy. In *Advances in the technology of stainless steels and related alloys*. ASTM International, 1965.
- [23] X. Xie, C. Xu, G. Wang, J. Dong, W.-D. Cao, and R. Kennedy. Ttt diagram of a newly developed nickel-base superalloy–allvac 718plus. *Superalloys*, 718(25):706, 2005.
- [24] W. Boesch and H. Canada. Precipitation reactions and stability of ni3nb in inconel alloy 718. *Journal of Metals*, 22:34–38, 1969.
- [25] W. Boesch and H. Canada. Precipitation reactions and stability of niscb in inconel 718 alloy. In *Seven Springs International Symposium*, 1968.
- [26] M. Fisk, J. Andersson, R. du Rietz, S. Haas, and S. Hall. Precipitate evolution in the early stages of ageing in Inconel 718 investigated using small-angle x-ray scattering. *Materials Science and Engineering: A*, 612:202–207, 2014.
- [27] M. Fisk and L.-E. Ion, J. C. and Lindgren. Flow stress model for in718 accounting for evolution of strengthening precipitates during thermal treatment. *Computational materials science*, 82:531–539, 2014.
- [28] M. Perez, M. Dumont, and D. Acevedo-Reyes. Implementation of classical nucleation and growth theories for precipitation. *Acta materialia*, 56(9):2119–2132, 2008.
- [29] M. Perez, M. Dumont, and D. Acevedo-Reyes. Corrigendum to “implementation of classical nucleation and growth theories for precipitation”[acta materialia 56 (2008) 2119–2132]. *Acta Materialia*, 57(4):1318, 2009.
- [30] A. Deschamps and M. Perez. Mesoscopic modelling of precipitation: A tool for extracting physical parameters of phase transformations in metallic alloys. *Comptes Rendus Physique*, 11(3-4):236–244, 2010.
- [31] M. Fisk, A. Lundbäck, J. Edberg, and J.M. Zhou. Simulation of microstructural evolution during repair welding of an in718 plate. *Finite Elements in Analysis and Design*, 120:92–101, 2016.
- [32] I.J. Moore, M.G. Burke, and E.J. Palmiere. Modelling the nucleation, growth and coarsening kinetics of γ'' (D0 22) precipitates in the Ni-base Alloy 625. *Acta Materialia*, 119:157–166, 2016.
- [33] I. J. Moore, M. G. Burke, N. T. Nuhfer, and E. J. Palmiere. Evaluation of classical precipitation descriptions for γ'' ni3nb d0₂₂ in Ni-base superalloys. *Journal of Materials Science*, 52(14):8665–8680, 2017.
- [34] R. Kampmann and R. Wagner. Kinetics of precipitation in metastable binary alloys-theory and application to cu-1.9 at% ti and ni-14 at% al. In *Decomposition of alloys: the early stages*, pages 91–103. Elsevier, 1984.
- [35] A. Drexler, B. Oberwinkler, S. Primig, C. Turk, E. Povoden-Karadeniz, A. Heinemann, W. Ecker, and M. Stockinger. Experimental and numerical investigations of the γ'' and γ' precipitation kinetics in Alloy 718. *Materials Science and Engineering: A*, 723:314–323, 2018.
- [36] M. R. Ahmadi, M. Rath, E. Povoden-Karadeniz, S. Primig, T. Wojcik, A. Danninger, M. Stockinger, and E. Kozeschnik. Modeling of precipitation strengthening in Inconel 718 including non-spherical γ'' precipitates. *Modelling and Simulation in Materials Science and Engineering*, 25(5):055005, 2017.
- [37] N. Zhou, D.C. Lv, H.L. Zhang, D. McAllister, F. Zhang, M.J. Mills, and Y. Wang. Computer simulation of phase transformation and plastic deformation in IN718 superalloy: Microstructural evolution during precipitation. *Acta Materialia*, 65:270–286, 2014.
- [38] D.C. Lv, D. McAllister, M.J. Mills, and Y. Wang. Deformation mechanisms of d0 22 ordered intermetallic phase in superalloys. *Acta Materialia*, 118:350–361, 2016.
- [39] D. McAllister, D. Lv, B. Peterson, H. Deutchman, Y. Wang, and M.J. Mills. Lower temperature deformation mechanisms in a γ'' -strengthened ni-base superalloy. *Scripta Materialia*, 115:108–112, 2016.
- [40] M.R. Ahmadi, B. Sonderegger, E. Povoden-Karadeniz, A. Falahati, and E. Kozeschnik. Precipitate strengthening of non-spherical precipitates extended in $\langle 100 \rangle$ or $\{100\}$ direction in fcc crystals. *Materials Science and Engineering: A*, 590:262–266, 2014.
- [41] M. R. Ahmadi, E. Povoden-Karadeniz, L. Whitmore, M. Stockinger, A. Falahati, and E. Kozeschnik. Yield strength prediction in ni-base alloy 718plus based on thermo-kinetic precipitation simulation. *Materials Science and Engineering: A*, 608:114–122, 2014.
- [42] M.R. Ahmadi, E. Povoden-Karadeniz, K.I. Öksüz, A. Falahati, and E. Kozeschnik. A model for precipitation strengthening in multi-particle systems. *Computational Materials Science*, 91:173–186, 2014.
- [43] D. Bardel, M. Perez, D. Nelias, A. Deschamps, C.R. Hutchinson, D. Maisonnnette, T. Chaise, J. Garnier, and F. Bourlier. Coupled precipitation and yield strength modelling for non-isothermal treatments of a 6061 aluminium alloy. *Acta Materialia*, 62:129–140, 2014.
- [44] D. Bardel, M. Fontaine, T. Chaise, M. Perez, D. Nelias, F. Bourlier, and J. Garnier. Integrated modelling of a 6061-t6 weld joint: From microstructure to mechanical properties. *Acta Materialia*, 117:81 – 90, 2016.
- [45] M. Gao and R.P. Wei. Grain boundary γ'' precipitation and niobium segregation in inconel 718. *Scripta metallurgica et materialia*, 32(7):987–990, 1995.
- [46] A. Niang. *Contribution à l'étude de la précipitation des phases intermétalliques dans l'alliage 718*. PhD thesis, Institut National Polytechnique de Toulouse, 2010.
- [47] G. Porod. General Theory. In O. Glatter and O. Kratky, editors, *Small-Angle X-Ray Scattering*, pages 17–51. Academic Press, London, 1982.
- [48] J. S. Pedersen. Analysis of small-angle scattering data from colloids and polymer solutions: Modeling and least-squares fitting. *Advances in Colloid and Interface Science*, 70:171–210, 1997.
- [49] M. Kotlarchyk and S.-H. Chen. Analysis of small angle neutron scattering spectra from polydisperse interacting colloids. *The Journal of Chemical Physics*, 79(5):2461–2469, 1983.
- [50] H. J. Wagner and A. M. Hall. Physical metallurgy of alloy 718. Technical report, BATTELLE MEMORIAL INST COLUMBUS OH DEFENSE METALS INFORMATION CENTER, 1965.
- [51] M. Perez. Gibbs–thomson effects in phase transformations. *Scripta materialia*, 52(8):709–712, 2005.
- [52] O.R. Myhr, Ø. Grong, and S.J. Andersen. Modelling of the age hardening behaviour of al–mg–si alloys. *Acta Materialia*, 49(1):65–75, 2001.
- [53] O.R. Myhr, Ø. Grong, H.G. Fjær, and C.D. Marioara. Modelling of the microstructure and strength evolution in al–mg–si alloys during multistage thermal processing. *Acta Materialia*, 52(17):4997–5008, 2004.
- [54] M. Hillert. The role of interfacial energy during solid-state phase

- transformations. *Jernkontorets Annaler*, 141:757–789, 1957.
- [55] M. Sundararaman, P. Mukhopadhyay, and S. Banerjee. Deformation behaviour of γ'' strengthened inconel 718. *Acta Metallurgica*, 36(4):847–864, 1988.
- [56] R.V. Pavil and G.B. Kale. Chemical diffusion of niobium in nickel. *J. Nucl. Mater.*, 230:57–60, 1996.
- [57] M. Karunaratne and R. Reed. Interdiffusion of niobium and molybdenum in nickel between 900-1300 °c. *Defect Diffusion Forum*, 237-240:420–425, 2005.
- [58] T. Ter-Ovanessian, C. Berrest, J. Deleume, J.-M. Cloué, and E. Andrieu. Influence of interstitials content on the diffusion of niobium in alloy 718. *Defect Diffusion Forum*, 289-292:161–166, 2009.
- [59] Z. K. Low, T. Chaise, D. Bardel, S. Cazottes, P. Chaudet, M. Perez, and D. Nelias. A novel approach to investigate delta phase precipitation in cold-rolled 718 alloys. *Acta Materialia*, 156:31–42, 2018.
- [60] Y.-F. Han, P. Deb, and M.C. Chaturvedi. Coarsening behaviour of γ'' -and γ' -particles in inconel alloy 718. *Metal Science*, 16(12):555–562, 1982.
- [61] M.K. Miller and S.S. Babu. Phase compositions in alloy 718: A comparison between apt/apfim measurements and thermodynamic predictions. In *Advanced Technologies for Superalloy Affordability, Proceedings of the 129th TMS Annual Meeting, TMS2000*, page 63, 2000.
- [62] Y. C. Fayman. Microstructural characterization and elemental partitioning in a direct-aged superalloy (DA 718). *Materials Science and Engineering*, 92:159–171, 1987.
- [63] M.G. Burke and M.K. Miller. Precipitation in Alloy 718: A combined AEM and APFIM Investigation. In *Superalloys 718, 625 and Various Derivatives (1991)*, pages 337–350. TMS, 1991.
- [64] D. Zhao, Y. Xu, S. Gouttebroze, J. Friss, and Y. Li. Modelling the age-hardening precipitation by a revised langer and schwartz approach with log-normal size distribution. *Metall. Mater. Trans. A*, 51:4838–4852, 2020.
- [65] J. Friedel. Dislocations, 1964.
- [66] U.F. Kocks, A. Argon, and M.F. Ashby. Thermodynamics and kinetics of slip (progress in materials science 19) ed b chalmers, jw christian and tb massalski, 1975.
- [67] A. Deschamps and Y. Brechet. Influence of predeformation and ageing of an al–zn–mg alloy—ii. modeling of precipitation kinetics and yield stress. *Acta Materialia*, 47(1):293–305, 1998.
- [68] Y. Mishima, S. Ochiai, N. Hamao, M. Yodogawa, and T. Suzuki. Solid solution hardening of nickel—role of transition metal and b-subgroup solutes—. *Transactions of the Japan institute of metals*, 27(9):656–664, 1986.
- [69] P. Donnadieu, M. Roux-Michollet, and V. Chastagnier. A quantitative study by transmission electron microscopy of nanoscale precipitates in al-mg-si alloys. *Philosophical Magazine A*, 79(6):1347–1366, 1999.
- [70] L.M. Brown and W. Stobbs. The work-hardening of copper-silica. *Philosophical Magazine*, 23(185):1201–1233, 1971.
- [71] J. F. Nie, B. C. Muddle, and I. J. Polmear. The effect of precipitate shape and orientation on dispersion strengthening in high strength aluminium alloys. In *Materials Science Forum*, volume 217, pages 1257–1262. Trans Tech Publ, 1996.
- [72] S. Esmaeili, D.J. Lloyd, and W.J. Poole. A yield strength model for the al-mg-si-cu alloy aa6111. *Acta Materialia*, 51(8):2243–2257, 2003.
- [73] A. Simar, Y. Brechet, B. De Meester, A. Denquin, and T. Pardoen. Sequential modeling of local precipitation, strength and strain hardening in friction stir welds of an aluminum alloy 6005a-t6. *Acta Materialia*, 55(18):6133–6143, 2007.
- [74] C. Gallais, A. Denquin, Y. Bréchet, and G. Lapasset. Precipitation microstructures in an aa6056 aluminium alloy after friction stir welding: Characterisation and modelling. *Materials Science and Engineering: A*, 496(1-2):77–89, 2008.
- [75] A. Simar, Y. Bréchet, B. De Meester, A. Denquin, C. Gallais, and T. Pardoen. Integrated modeling of friction stir welding of 6xxx series al alloys: Process, microstructure and properties. *Progress in Materials Science*, 57(1):95–183, 2012.
- [76] M. Fukuhara and A. Sanpei. Elastic moduli and internal frictions of inconel 718 and ti-6al-4v as a function of temperature. *Journal of materials science letters*, 12(14):1122–1124, 1993.
- [77] J.M. Oblak, D.S. Duvall, and D.F. Paulonis. An estimate of the strengthening arising from coherent, tetragonally-distorted particles. *Materials Science and Engineering*, 13(1):51–56, 1974.
- [78] M. Sundararaman, J.B. Singh, and P. Mukhopadhyay. Estimation of order strengthening in inconel 718 type alloys containing all $[\gamma]'$ precipitate variants. *Scripta Metallurgica et Materialia*, 29(4), 1993.